SCIENTIFIC REPORTS

OPEN

SUBJECT AREAS:
ELECTRONIC PROPERTIES AND MATERIALS
NANOSCALE MATERIALS
NANOWIRES
ELECTRONIC DEVICES

Received
18 December 2012

Accepted
28 February 2013

Published
28 March 2013

Correspondence and requests for materials should be addressed to M.T. (tianml@hmfl.ac.cn)

One-dimensional weak antilocalization in single-crystal Bi_2Te_3 nanowires

Wei Ning[1,2], Haifeng Du[1,2], Fengyu Kong[1,2], Jiyong Yang[1,2], Yuyan Han[1,2], Mingliang Tian[1,2,3] & Yuheng Zhang[1,2]

[1]High Magnetic Field Laboratory, Chinese Academy of Science, Hefei 230031, Anhui, P. R. China, [2]Hefei National Laboratory for Physical Science at The Microscale, University of Science and Technology of China, Hefei 230026, People's Republic of China, [3]The Center for Nanoscale Science and Department of Physics, The Pennsylvania State University, University Park, Pennsylvania 16802-6300.

Angle-dependent magnetoconductance was measured on an individual surface-curved Bi_2Te_3 single-crystal nanowire fabricated by electrochemical deposition, where the evolution of surface conduction with wire diameters was investigated. It was found that the magnetoconductance of these nanowires in low field regime can be well described by one-dimensional (1D) weak antilocalization (WAL) model, where the dephasing length of the electrons follows $T^{-1/3}$ dependence but insensitive to the wire diameter. Meanwhile, such a 1D surface WAL was found to be enhanced significantly with the decrease of the wire diameter.

Topological insulator (TI) is a new state of matter. It is characterized by a full insulating gap in the bulk and gapless spin-resolved surface state (SS) in which the spin of the electrons is locked perpendicular to its momentum by the strong spin-orbit interaction. These spin helical properties of Dirac fermions in SS have made them relevant for exotic new physics[1–3] and applications on improved spintronic devices and potentially useful for quantum computing[4–7]. In three-dimensional (3D) TIs, the topological surface states have been proved by angle-resolved photoemission spectroscopy (ARPES)[8,9], scanning tunneling microscopy[10,11] and electrical transport measurements including two-dimensional (2D) weak antilocalization (WAL)[12–17], Shubnikov-de Haas (SdH) or quantum Hall (QH) effect[18], where a 2D character was determined due to a fact that all of these effects were found only sensitive to the perpendicular component of the magnetic field. However, direct probing the surface state of an individual nanowire by ARPES is almost impossible because of the limitation of sample size. Instead, electrical transport measurement become the most efficient way to obtain the surface information due to its unique geometry and extreme large surface to volume ratio[19,20]. Several quasi-1D nanoribbons have been synthesized, including Bi_2Se_3, Bi_2Te_3 and $Bi_2(Se_xTe_{1-x})_3$[21–25], where the Aharonov-Bohm and Atshuler-Aronov-Spivak[20,21], Aharonov-Casher effect[22] and 2D WAL of the SS[23,25] were found. Compared with the TI nanoribbons with two well-defined parallel surfaces, the nature of the surface state in a surface-curved 1D cylindrical nanowire has not been well explored experimentally although a number of unique and fascinating properties[26–28] have been predicted theoretically, such as the possible helical Luttinger liquid[28] that was ever described as the edge mode of the 2D quantum spin Hall (QSH) topological insulator.

In this work, we report angle-dependent magnetoresistance (MR) studies on an individual surface-curved Bi_2Te_3 nanowire fabricated by electrochemical deposition. The evolution of the surface conduction with wire diameters was carefully investigated. It was found that the nanowires of different diameters showed similar positive MR behavior, where the variations of their magnetoconductance at different angles, $\Delta G(\theta,B)$, by subtraction of the magnetoconduction at $\theta = 0^\circ$ can be surprisingly normalized to one curve with the perpendicular component, $B_\perp = B\sin\theta$, of the magnetic field, where θ is the angle between B and the wire axis as shown schematically in the inset of Fig. 3(a). Such a behavior is a direct indication of the WAL of the surface states of nanowire. Theoretical analysis based on the WAL model showed that the dephasing length of electrons in these thin curved nanowires follows $T^{-1/3}$ temperature dependence but insensitive to the wire diameter, indicating the 1D WAL character from the surface channels of the nanowire instead of the expected 2D WAL reported in nanoribbons[23,25] and bulk[12–15]. These results are also consistent with our observation that the upper limit for the range of the magnetic fields which is appropriate for fitting the observed 1D WAL increases significantly with the decrease of the wire diameter, *i.e.*, an enhancement of quasi-one dimensionality in electrical transport of surface states in small diameter wire.

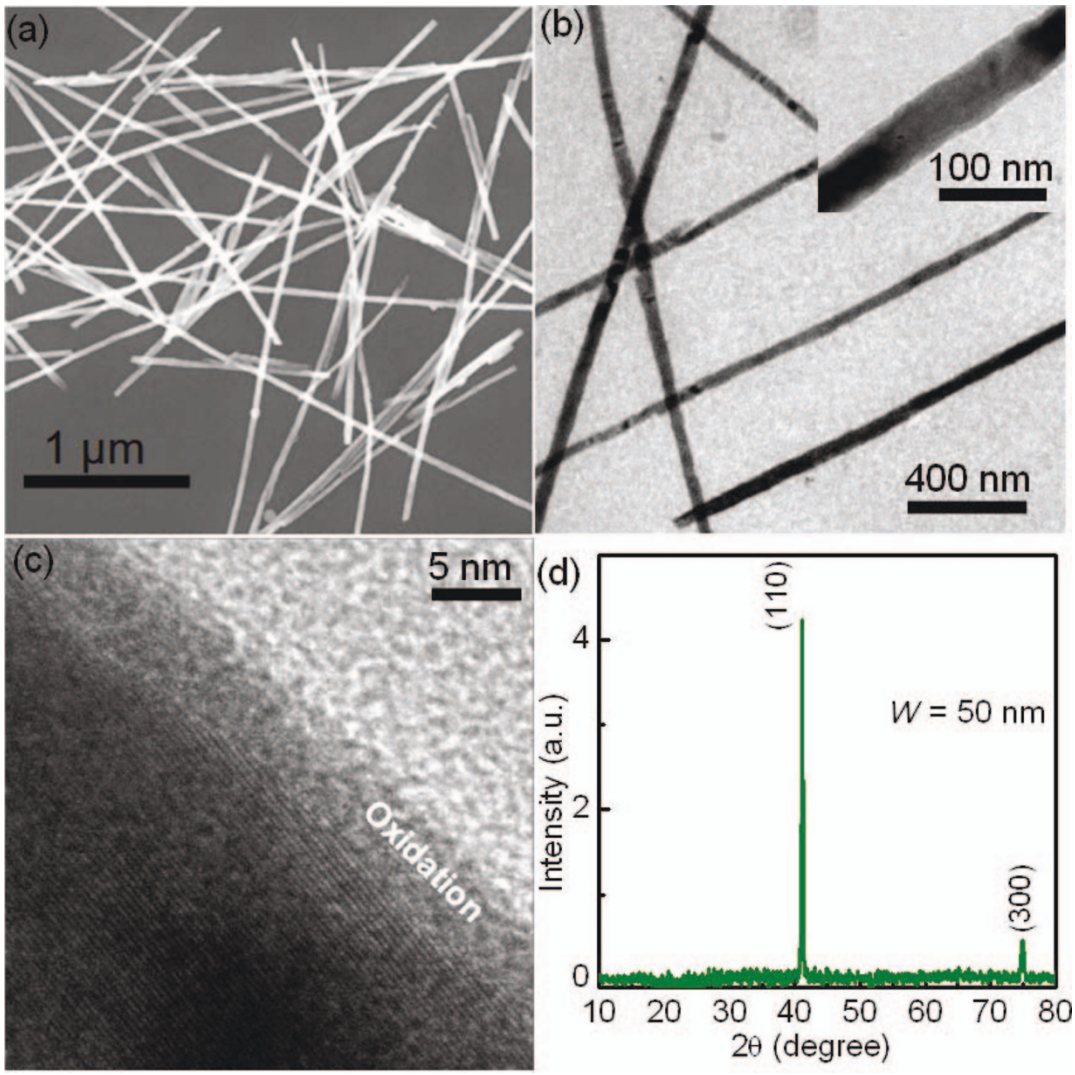

Figure 1 | (a) and (b) are respectively the low magnification SEM and TEM images of nanowires with $W = 50$ nm. The inset of (b) shows an enlargement of an individual nanowire. (c) High-resolution TEM image of 50 nm wire selected randomly. An oxidation layer of approximately ~5.0 nm is visible on the surface. (d) x-ray diffrtaction spectra carried out on the nanowire arrays, where the (110) diffraction is the dominant peak in the spectra.

Results

All of Bi_2Te_3 nanowires used in this work were synthesized by electrochemical deposition via customer-made porous anodic aluminum oxide (AAO) membrane. The wire diameter was exactly controlled by the pore size of the template[29] so that we are able to carry out a systematic comparative study on wires of various diameters by selecting the templates with proper pore size. While the diameter of each wire along its length is uniform, it shows variations from wire to wire within an uncertainty of ~20%, verified by both scanning electron microscopy (SEM) and transmission electron microscopy (TEM). It was shown that the majority of the nanowires have a length of 8~15 μm with single-crystal morphology as shown in Figs. 1 (a), 1(b) and 1(c). An oxidation layer of approximately ~5.0 nm, which was probably formed after the nanowires were released from the membrane, is visible on the surface. All samples of different diameters, such as 300 nm, 100 nm and 50 nm fabricated under the same controlled conditions showed very similar structure, verified by x-ray diffraction measurements on the nanowire arrays (see Fig. 1d), where the (110) diffraction is the dominant peak in the spectra.

Standard 4-probe transport measurements were carried out on an individual nanowire using a physical property measurement system (PPMS). Four platinum (Pt) strips of 100 nm (width) × 100 nm (thickness) as shown in the lower inset of Fig. 2 (a) were deposited onto the wire as the contact electrodes using FEI Helios NanoLab 600i FESEM/FIB dual beam system. Resistance as a function of temperature for three individual Bi_2Te_3 nanowires of 300 nm, 100 nm and 50 nm showed very similar transport behavior in high temperature range (see Fig. 2a), such as a resistance hump near 220 K and a subsequent metallic behavior down to ~25 K. We noticed that the hump behavior of the resistance usually appears in TI-samples with the reduction of bulk carrier density less than $10^{17}/cm^3$ by element-doping (e.g., Na[30], Pb[16] or Sb[18] doping and so on), where the surface contribution to the total conduction become significant. Therefore, the similar hump behavior observed in our nanowires might have the same origin due to the competition of conduction between the surface and bulk. When the temperature decreases, the contribution of the bulk conductivity decreases sharply and thus the surface conductivity will be dominant in low-T range. Below about 25 K, both larger diameter wires (W = 100 nm and 300 nm) show slightly an upturn in resistance while the small diameter wire (W ~ 50 nm) displays a plateau down to 2 K. It was also noted that the upturn behavior becomes more significant with the increase of the wire diameter, as shown in the upper inset of Fig. 2 (a). The tendency of the weakened insulating feature with the decrease of the wire diameter at low temperatures means that the contribution of the metallic surface states to the total conduction might be enhanced in such a thinner nanowire.

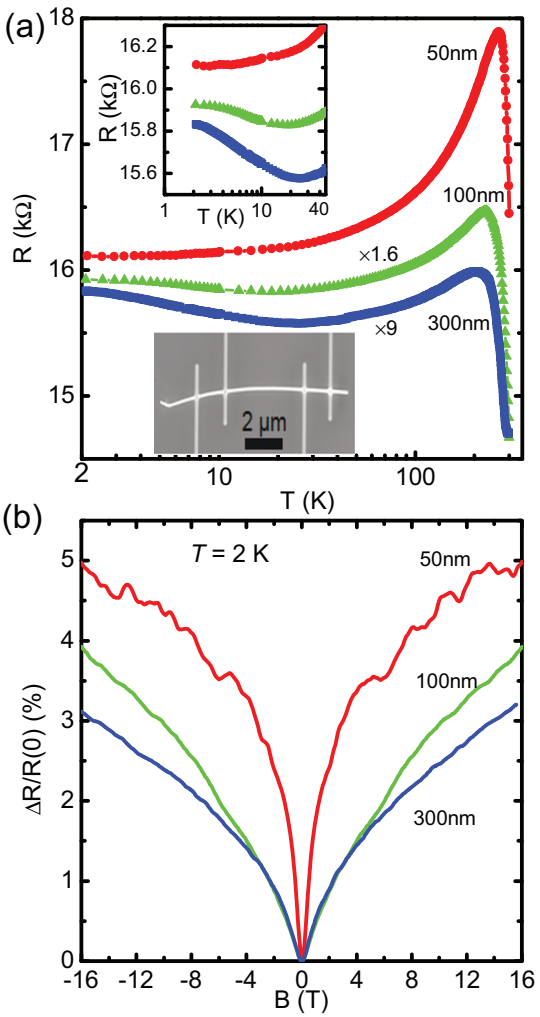

Figure 2 | (a) Resistance versus temperature for three nanowires of $W = 300$ nm, 100 nm and 50 nm. The upper inset shows the resistance in low temperatures. The lower inset is the SEM image of the four-probe configuration of wire for transport measurement. (b) Normalized magnetoresistance in perpendicular magnetic field for W = 50 nm, 100 nm and 300 nm wires. The MR oscillations superimposed on the positive MR curves were observed. The amplitude of the MR oscillations was enhanced when the diameter decreases from 300 nm to 50 nm.

Fig. 2 (b) shows the normalized resistance as a function of the magnetic field aligned perpendicular to the axis of the nanowires at $T \sim 2$ K. The MR quantum oscillations or fluctuations were seen in all three diameter wires but the amplitude of the oscillations in 50 nm wire was much larger than those of 100 nm or 300 nm wires, which is consistent with our expectation that the metallic surface contribution is probably enhanced in thinner nanowires due to the high ratio of the surface to bulk volume. The details related to the nature of these quantum oscillations in high field regime has been discussed elsewhere[31]. Here we focused our attention on the MR behavior in low-H regime.

The overall MR behavior as shown in Fig. 2 (b) is very similar to those reported in TI-bulk, films and nanoribbons, namely all three wires display a positive MR over entire magnetic field regime we measured and a valley in low-H range. Such a positive MR in TIs was usually attributed to the weak antilocalization (WAL) of the surface states because of the strong spin-orbit coupling and the helicity of the surface states[32,33]. The WAL is a negative quantum correction to the classical weak localization due to the wave nature of the electrons in a disordered metallic system.

Discussion

To quantitatively understand the size dependent properties of the MR in these thin surface-curved TI nanowires, Figure 3 (a), 3(c) and 3(e), respectively, show the angle-dependent magnetoconductance, $G(\theta,B) = 1/R(\theta,B)$, of three samples with diameters of $W = 300$ nm, 100 nm and 50 nm. It was known that the WAL induced by 2D surface states is characterized by a sole dependence on the perpendicular component, $B_\perp = B\sin(\theta)$, of the applied field. The fact is that, as usually expected the magnetoconductance of surface state at $\theta = 90^\circ$, the magnetoconductance at $\theta = 0^\circ$ was also observed, indicating that bulk electrons also contribute to the total conductance. Therefore, to extract the pure surface state contribution, we subtract the 3D WAL contribution at $\theta = 0^\circ$ from the total magnetoconductance at various angles, i.e., $\Delta G(\theta,B) = G(\theta,B) - G(0,B)$, with $G(\theta,B) = 1/R(\theta,B)$ and $G(0,B) = 1/R(0,B)$. Figs. 3(b), 3(d) and 3(f) show $\Delta G(\theta,B)$ versus $B_\perp = B\sin(\theta)$ for nanowires with $W = 300$ nm, 100 nm and 50 nm, respectively. The surprising feature is that all of the traces at various angles can be approximately normalized to a single curve in low field regime although the angle θ defined here has an uncertainty of at least ± 5 degree. These results clearly indicate that the magnetoconductance shown in Figs. 3 (b), 3(d) and 3(f) is mainly a result of the surface conductivity.

We now turn to a more quantitative analysis of the WAL behavior. As we noticed from Fig. 3 that the magnetoconductance of the surface states in 300 nm large diameter wire display a cusp-like shape while a parabolic-like shape was obtained with the decrease of the wire diameter. The cusp-like shape of the surface magnetoconductance was always seen in bulk and thin film TIs, where a 2D WAL dominates in the surface state. Because the typical dephasing length in TIs is usually on the order of $L_\varphi \sim 330$ nm[14], which is larger than the diameter of our Bi_2Te_3 nanowires ($d = 300 \sim 50$ nm), a quasi-1D localization theory was used to fit the observed WAL. In a 1D system, the weak localization correction at a magnetic field B that includes the electron-electron (e-e) interactions and spin-orbit (s-o) interactions to the conductance is given by[34,35]:

$$\Delta G = \frac{\sqrt{2}e^2}{\pi\hbar}\frac{L_n}{L}\left[\frac{3}{2}\frac{A_i\left(\frac{2L_n^2}{L_1}\right)}{A_i'\left(\frac{2L_n^2}{L_1}\right)} - \frac{1}{2}\frac{A_i\left(\frac{2L_n^2}{L_2}\right)}{A_i'\left(\frac{2L_n^2}{L_2}\right)}\right] \quad (1)$$

where ΔG is the conductance quantum correction in 1D, L and L_n are the wire length and the Nyquist length, respectively, A_i represents the Airy function, $L_1 = (4/3L_{so}^2 + L_\varphi^2)^{-1/2}$, and $L_2 = \left(1/L_\varphi^2 + W^2/3L_H^2\right)^{-1/2}$. Here, $L_{so} = \sqrt{D\tau_{so}}$ is the spin-orbit length that characterizes the strength of spin-orbit coupling, where D is the diffusion constant. $L_\varphi = \sqrt{D\tau_\varphi}$, $L_H = (\hbar/eB)^{1/2}$ are the dephasing length and the magnetic length, W is the diameter of the wire.

Considering the oxide layer of nanowires, the actual widths, W, of the three wires quoted by 300 nm, 100 nm, and 50 nm were selected as 290 nm, 90 nm and 40 nm in the theoretical fitting, respectability. The solid red curves in Fig. 3(b), 3(d) and 3(f) are the fitting results with 1D localization theory, yielding $L_n = 27.1$ nm, $L_\varphi = 396.0$ nm, $L_{so} = 20.8$ nm for nanowire of 300 nm, $L_n = 34.8$ nm, $L_\varphi = 395.9$ nm, $L_{so} = 26.1$ nm for nanowire of 100 nm, and $L_n = 34.0$ nm, $L_\varphi = 400.1$ nm, $L_{so} = 25.9$ nm for nanowire of 50 nm. It was noted that $L_{so} << L_\varphi$, which means the spin-orbit scattering time τ_{so} is significantly shorter than τ_φ, being consistent with the results obtained from other similar topological insulators[17,36]. Obviously, the fitting is more successful for small diameter wire, and the upper limit for the range of the magnetic field which is appropriate for the 1D WAL increases significantly with the decrease of the wire diameter. Since the dephasing length L_φ shows no clear diameter dependence, indicating the surface nature of the 1D WAL (If the bulk contribution to the WAL effect were significant, L_φ should change with the diameter). These observations are consistent

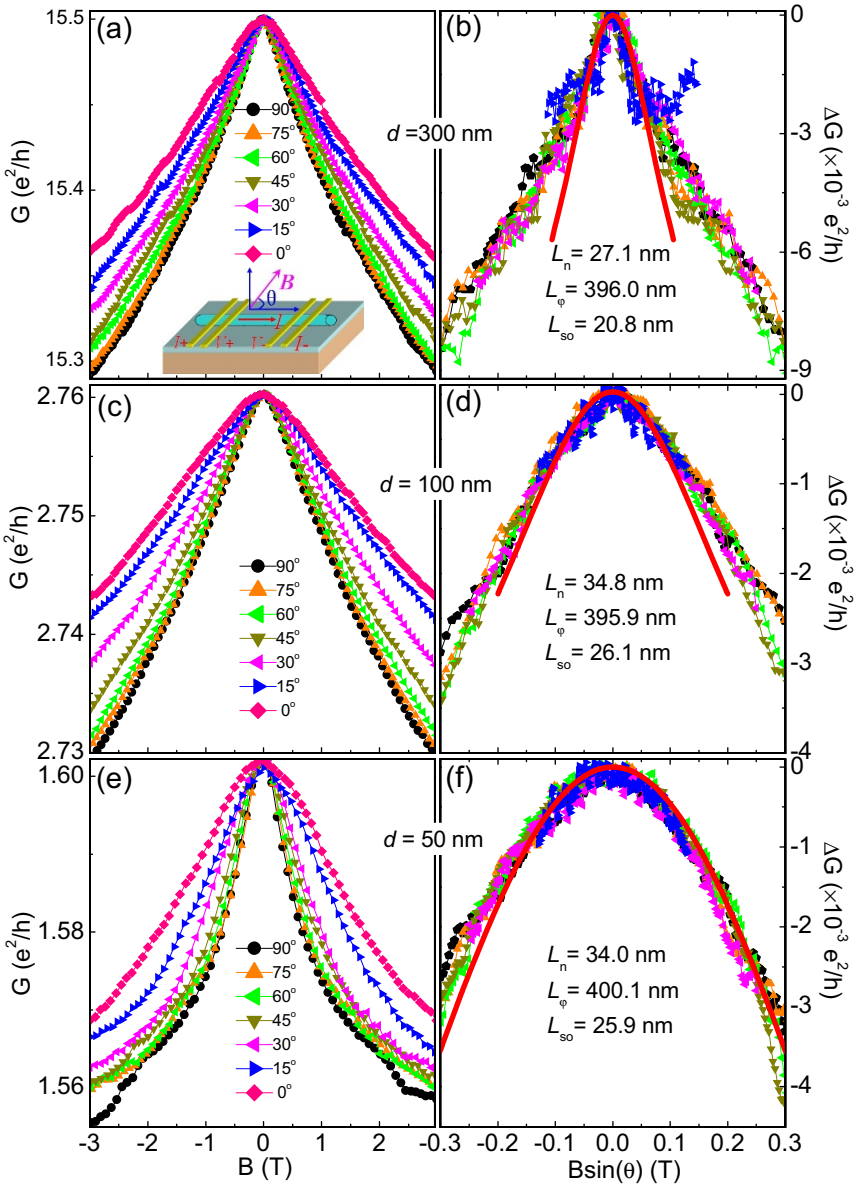

Figure 3 | (a), (c) and (e) are respectively the angle-dependent magnetoconductance of Bi_2Te_3 nanowires (W = 300 nm, 100 nm and 50 nm) measured at 2 K. The magnetoconductance persists at $\theta = 0^\circ$, indicating the contribution of bulk electrons to the WAL due to the bulk spin-orbit coupling. Inset: schematic of the measurement setup where θ denotes the angle between the direction of the magnetic field and the current flow in the nanowires. (b), (d) and (f) are respectively the magnetoconductance change plotted in the perpendicular component, Bsinθ, of the magnetic field for nanowires of $W = 300$, 100 and 50 nm by subtracting the bulk contribution of the WAL at $\theta = 0^\circ$. The solid red lines are the fit with 1D localization theory. All the traces were normalized to a single curve in low field range, indicating the surface nature of the magnetoconductance. The upper limit for the range of the magnetic field which is appropriate for fitting the 1D WAL increases significantly with the decrease of the wire diameter.

with our expectation that quasi-one dimensionality in electrical transport of surface state is significantly enhanced in small diameter wire. A deviation of the 1D WAL fitting for 300 nm wire can be understood from a fact that the 300 nm is almost comparable to the phase coherence length, L_φ. We have also tried the fitting with 2D WAL model for 300 nm wire, but unfortunately we obtained unphysical small fitting parameters compared with those reported for TI- bulk or film samples. A possible reason might be related to its cylindrical geometry with a curved surface or the diameter of 300 nm is just on the order of between 1D and 2D dimensionality.

To further investigate the observed WAL, the magnetoconductance as a function of temperature was also measured in several other Bi_2Te_3 nanowires of different diameters (W = 50 nm, 100 nm and 300 nm) in the field aligned perpendicular to the wire axis, as shown in Figs. 4 (a), 4(c) and 4(e), respectively. As T increases, the cusp of the magnetoconductance in low field range is gradually broadened and finally disappears. Fitting the data at different T with eq.(1), the observed characteristic lengths of L_n, L_φ and L_{so} as a function of temperatures are shown in Fig. 4 (b), 4(d) and 4(f) for nanowires with W = 50 nm, 100 nm and 300 nm, respectively. All characteristic lengths decrease with the increase of temperatures due to the increased thermal scattering.

It was well-known that the Nyquist length L_n and coherence length L_φ are proportional to $T^{-1/2}$ for the two dimensional system and $T^{-1/3}$ for the one-dimensional one[24,30,37]. Fig. 4(b) shows that the Nyquist length L_n, coherence length L_φ and spin-orbit length L_{so} for 50 nm wire are proportional to $T^{-0.37}$, $T^{-0.32}$ and $T^{-0.37}$ which are very close to the exponent, −1/3, expected for the one-dimensional system, i.e., the electron conduction in Bi_2Te_3 nanowires follows the quasi-one-dimensionality. Similar fitting were also done for nanowires with

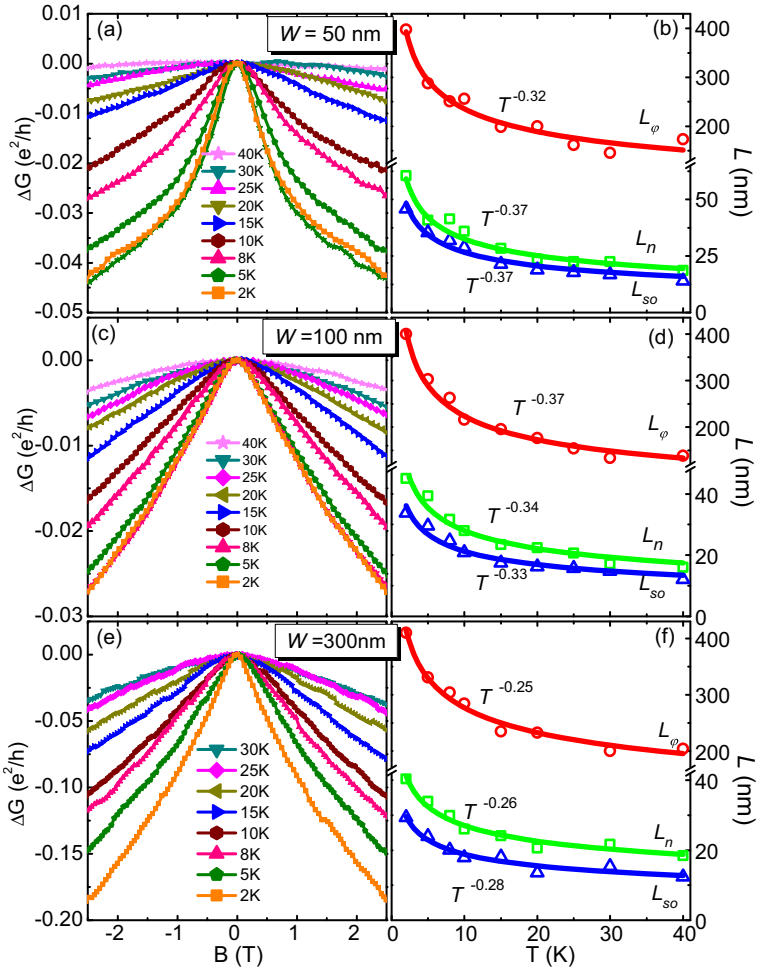

Figure 4 | (a), (c) and (e) respectively show magnetoconductance at different temperatures with magnetic fields aligned perpendicular to the wire axis for nanowires with W = 50 nm, 100 nm and 300 nm. (b), (d) and (f) respectively show the characteristic lengths of L_n, L_φ and L_{so} as a function of temperatures obtained from the fitting with the 1D localization theory. The solid lines in each plot show the power-law dependence on temperatures, yielding L_n, L_φ and L_{so} decay as $\sim T^{-0.37}$, $T^{-0.32}$, $T^{-0.37}$ for 50 nm wire, and $T^{-0.34}$, $T^{-0.37}$, $T^{-0.33}$ for 100 nm wire, and $T^{-0.26}$, $T^{-0.25}$, $T^{-0.28}$ for 300 nm wire. The exponent of L_n and L_φ closes to $-1/3$ expected for the one-dimensionality in Bi_2Te_3 nanowires.

W = 100 nm and 300 nm. The obtained results indicate that L_n, L_φ and L_{so} decay as $\sim T^{-0.34}$, $T^{-0.37}$, and $T^{-0.33}$ for W = 100 nm, and $T^{-0.26}$, $T^{-0.25}$, $T^{-0.28}$ for W = 300 nm, as shown in Fig. 4 (d) and 4 (f), respectively. It is noted that, as shown in Fig. 4(f), $L_\varphi < W$ at $T >$ 10 K for nanowires with W = 300 nm, which indicates that the transport behavior of electrons is beyond quasi-one-dimensional channel, but two or three dimensionally above this temperature.

In summary, single crystal Bi_2Te_3 nanowires with diameters arranging from 50 nm to 300 nm were fabricated by electrodeposition. Both MR oscillations and weak antilocalization (WAL) behavior were observed for nanowires with different diameters, and both properties were enhanced with the decrease of wire diameters, indicating the enhancement of surface states in thinner nanowires. The obtained dephasing length L_φ shows independence of diameter but follows $T^{-1/3}$ dependence, suggesting the quasi-one-dimensional nature of magnetoconductance in the surface curved Bi_2Te_3 nanowires.

Methods

Synthesis. Bi_2Te_3 nanowires were fabricated by direct-current electrodeposition into porous anodic aluminum oxide membrane (AAO). The plating solution was prepared by dissolving 10 mM Te (powder: 99.9998% purity) and 7.5 mM Bi (shots: 99.999% purity) elements into concentrated nitric acid (69.1%), and then the solution was diluted to 1 M final concentration with distilled water[38]. The electrodeposition was carried out at a constant potential of −62 mV, relative to an Ag/AgCl reference electrode at room temperature. A pure Pt-wire was used as the counter electrode and Au film evaporated on one side of the AAO membrane prior to the electrodeposition was used as the working electrode. Freestanding nanowires were obtained by dissolving the membrane with 2 M aqueous NaOH solution, followed by precipitating the wires via centrifugation.

Device fabrication and characterization. To make standard four-probe devices on an individual Bi_2Te_3 NW for transport measurement, we dispersed the NWs on a silicon substrate with a 1 μm thick Si_3N_4 insulating layer. Then, the sample was transferred into FEI NanoLab 600i SEM/FIB dual beam system for the deposition of Pt-electrodes. The size of the four Pt-stripe electrodes has a nominal width of 100 nm and a thickness of 100 nm deposited. Usually, the film by FIB-induced Pt deposition is amorphous consisting of Pt, C, Ga or O depending on the deposition condition. While the maximum spreading or diffusion distance of the actual Pt along the wire is on the order of 300 nm, the distance (L) between the inner edges of the two voltage electrodes for all of the studied samples was kept larger than 4 μm, which is much longer than the spreading distance.

1. Fu, L. & Kane, C. L. Probing neutral Majorana fermion edge modes with charge transport. *Phys. Rev. Lett.* **102**, 216403 (2009).
2. Zhang, D. *et al.* Superconducting proximity effect and possible evidence for Pearl vortices in a candidate topological insulator. *Phys. Rev. B* **95**, 165120 (2011).
3. Wang, J. *et al.* Interplay between topological insulators and superconductors. *Phys. Rev. B* **85**, 045415 (2012).
4. Fu, L., Kane, C. L. & Mele, E. J. Topological insulators in three dimensions. *Phys. Rev. Lett.* **98**, 106803 (2007).
5. Qi, X. L. & Zhang, S. C. Topological insulators and superconductors. *Rev. Mod. Phys.* **83**, 1057–1110 (2011).
6. Bernevig, B. A., Hughes,T. L. & Zhang, S. C. Quantum spin Hall effect and topological phase transition in HgTe quantum well. *Science* **314**, 1757–1761 (2006).

7. Hasan, M. Z. & Kane, C. L. Colloquium: Topological insulators. *Rev. Mod. Phys.* **82**, 3045 (2010).
8. Xia,Y. *et al.* Observation of a large-gap topological insulator class with a single Dirac cone on the surface. *Nat. Phys.* **5**, 398–402 (2009).
9. Hsieh, D. *et al.* A tunable topological insulator in the spin helical Dirac transport regime. *Nature* **460**, 1101–1105 (2009).
10. Zhang, T. *et al.* Experimental demonstration of topological surface states protected by time-reversal symmetry. *Phys. Rev. Lett.* **103**, 266803 (2009).
11. Roushan, P. *et al.* Topological surface states protected from backscattering by chiral spin texture. *Nature* **460**, 1106–1109 (2009).
12. Bao, Li *et al.* Weak antilocalization and quantum oscillations of surface states in topological insulator Bi_2Se_2Te. *Sci. Rep.* **2**, 726 (2012).
13. Li, Z. *et al.* Two-dimensional universal conduction fluctuations and the electron-phonon interaction of surface states in Bi_2Te_2Se miscroflakes. *Sci. Rep.* **2**, 595 (2012).
14. He, H. T. *et al.* Impurity effect on weak antilocalization in the topological insulator Bi_2Te_3. *Phys. Rev. Lett.* **106**, 166805 (2012).
15. Matsuo, S. *et al.* Weak antilocalization and conductance fluctuation in a submicrometer-sized wire of epitaxial Bi_2Se_3. *Phys. Rev. B.* **85**, 075440 (2012).
16. Wang, J. *et al.* Evidence for electron-electron interaction in topological insulator thin films. *Phys. Rev. B* **83**, 245438 (2011).
17. Wang, J. *et al.* Anomalous anisotropic magnetoresistance in topological insulator films. *Nano Res.* **5**, 739–746 (2012).
18. Analytis, J. G. *et al.* Two-dimensional surface state in the quantum limit of a topological insulator. *Nat. Phys.* **6**, 960 (2010).
19. Tang, H., Liang, D., Qiu, R. L. J. & Gao, X. P. A. Two-dimensional transport-induced linear magneto-resistance in topological insulator Bi_2Te_3 nanoribbons. *ACS Nano* **5**, 7510–7516 (2011).
20. Xiu, F. *et al.* Manipulating surface states in topological insulator nanoribbons. *Nat. Nanotech.* **6**, 216–221 (2011).
21. Peng, H. L. *et al.* Aharonov-Bohm interference in topologcial insulator nanoribbons. *Nature Mater.* **9**, 225–229 (2010).
22. Qu, F. *et al.* Aharonov-Casher effect in Bi_2Se_3 square-ring interferometers. *Phys. Rev. Lett.* **107**, 016802 (2011)
23. Cha, J. J. *et al.* Magnetic doping and Kondo effect in Bi_2Se_3 nanoribbons. *Nano Lett.* **10**, 1076–1081 (2010).
24. Cha, J. J. *et al.* Weak antilocalization in $Bi_2(Se_xTe_{1-x})_3$ nanoribbons and nanoplates. *Nano Lett.* **12**, 1107–1111 (2012).
25. Cha, J. J. *et al.* Effects of magnetic doping on weak antilocalization in narrow Bi_2Se_3 nanoribbons. *Nano Lett.* **12**, 4355–4359 (2012).
26. Bardarson, J. H., Brouwer, P. W. & Moore, J. E. Aharonov-Bohm Oscillations in Disordered Topological Insulator Nanowires. *Phys. Rev. Lett.* **105**, 156803 (2010).
27. Zhang, Y. & Vishwanath, A. Anomalous Aharonov-Bohm conductance oscillations from topological insulator surface states. *Phys. Rev. Lett.* **105**, 206601 (2010).
28. Egger, R., Zazunov, A. & Yeyati, A. L. Helical Luttinger liquid in topological insulator nanowires. *Phys. Rev. Lett.* **105**, 136043 (2010).
29. Tian, M. L. *et al.* Penetrating the oxide barrier in situ and separating freestanding porous alumina films in one step. *Nano Lett.* **5**, 697–703 (2005).
30. Wang, Y. *et al.* Gate-controlled surface conduction in Na-doped Bi_2Te_3 topological insulator nanoplates. *Nano Lett.* **12**, 1170–1175 (2012).
31. Tian, M. L. *et al.* Dual evidence of surface Dirac states in thin cylindrical topological insulator Bi_2Te_3 nanowires. *Sci. Rep.* **3**, 1212 (2013).
32. Hikami, S., Larkin, A. I. & Nagaoka, Y. Spin-orbit interaction and magnetoresistance in the two dimensional random system. *Prog. Theor. Phys.* **63**, 707–710 (1980).
33. Suzuura, H. & Ando, T. Crossover from symplectic to orthogonal class in a two-Dimensional honeycomb lattice. *Phys. Rev. Lett.* **89**, 266603 (2002).
34. Altshuler, B. L., Aronov, A. G. & Khmelnitsky, D. E. Effects of electron-electron collisions with small energy transfers on quantum localization. *J. Phys. C* **15**, 7367–7386 (1982).
35. Echternach, P. M., Gershenson, M. E. & Bozler, H. M. Nyquist phase relaxation in one-dimensional metal films. *Phys. Rev. B* **48**, 11516 (1993).
36. Steinberg, H. *et al.* Electrically tunable surface-to-bulk coherent coupling in topological insulator thin films. *Phys. Rev. B* **84**, 233101 (2011).
37. Altshuler, B. L. & Aronov, A. G. Electron-electron interaction in disordered systems. Vol. 10, (Elsevier, New York, 1985).
38. Martín-Gonzaález, M. S., Prieto, A. L., Gronsky, R., Sands, T. & Stacya, A. M. Insight into the electrodeposition of Bi_2Te_3. *J. Electrochem. Soc.* **149**, C546–C554 (2002).

Acknowledgments

This work was supported by the National Key Basic Research of China, under Grant Nos. 2011CBA00111 and 2010CB923403; the National Nature Science Foundation of China, Grant No. 11174292, 11104281 and 11104280; the Anhui Natural Science Foundation of China, Grant No. 11040606M08; the Knowledge Innovation Program of the Chinese Academy of Sciences, Grant No. Y06CSI1121B2Q and the Hundred Talents Program of the Chinese Academy of Science.

Author contributions

M.T. supervised the research. W.N., H.D., Y.H., F.K. and J.Y. synthesized the Bi_2Te_3 nanowires, fabricated the devices and carried out the transport measurement in high magnetic field and performed structural analysis. Y.Z. contributed to the analysis. W.N. and M.T. wrote the paper, together with the help of all other co-authors.

Additional information

Competing financial interests: The authors declare no competing financial interests.

How to cite this article: Ning, W. *et al.* One-dimensional weak antilocalization in single-crystal Bi_2Te_3 nanowires. *Sci. Rep.* **3**, 1564; DOI:10.1038/srep01564 (2013).